The Journal of Chemical Physics

RESEARCH ARTICLE | OCTOBER 22 2025

# Thermal neutron cross sections of aluminum and magnesium fluorides and quantum kinetic energy of fluorine

Margherita Simoni ; Setareh Fatemi ; Lorenzo Airoldi ; Silva Bortolussi ; Mattia Gaboardi ; Matthew Krzystyniak ; Anna Marsicano ; Triestino Minniti ; Ignacio Porras ; Ian Postuma ; Ricardo Ramos ; Roberto Senesi ; Umberto Anselmi Tamburini ; Valerio Vercesi ; Giovanni Romanelli



*J. Chem. Phys.* 163, 164503 (2025)
https://doi.org/10.1063/5.0294270



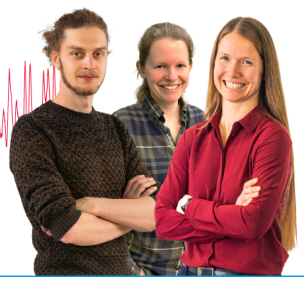

The Journal of Chemical Physics ARTICLE pubs.aip.org/aip/jcp

# Thermal neutron cross sections of aluminum and magnesium fluorides and quantum kinetic energy of fluorine

Cite as: J. Chem. Phys. 163, 164503 (2025); doi: 10.1063/5.0294270
Submitted: 2 August 2025 • Accepted: 27 September 2025 •
Published Online: 22 October 2025



Margherita Simoni,[1] Setareh Fatemi,[2,a)] Lorenzo Airoldi,[3] Silva Bortolussi,[2,4] Mattia Gaboardi,[1,a)] Matthew Krzystyniak,[5] Anna Marsicano,[5] Triestino Minniti,[1] Ignacio Porras,[6] Ian Postuma,[2] Ricardo Ramos,[2] Roberto Senesi,[1,7] Umberto Anselmi Tamburini,[2,3] Valerio Vercesi,[2] and Giovanni Romanelli[1,5]

## AFFILIATIONS

[1] Physics Department and NAST Centre, Università degli Studi di Roma Tor Vergata, via della Ricerca Scientifica 1, 00133 Roma, Italy
[2] National Institute of Nuclear Physics (INFN), Unit of Pavia, via A. Bassi 6, Pavia 27100, Italy
[3] Department of Chemistry, University of Pavia, V.le Taramelli 12, Pavia I27100, Italy
[4] Department of Physics, University of Pavia, via A. Bassi 6, Pavia 27100, Italy
[5] ISIS Neutron and Muon Source, Rutherford Appleton Laboratory, Chilton OX110QX, United Kingdom
[6] Department of Atomic, Molecular and Nuclear Physics, University of Granada, Avenida de Fuentenueva S/N, CP:18071 Granada, Spain
[7] Istituto di Struttura della Materia (ISM), Consiglio Nazionale delle Ricerche, Via del Fosso del Cavaliere, 100, Rome 00133, Italy

[a)] **Authors to whom correspondence should be addressed:** setareh.fatemi@pv.infn.it and mattia.gaboardi@uniroma2.it

## ABSTRACT

We provide the modeling and experimental validation of thermal neutron cross sections, including scattering and absorption contributions, of aluminum fluoride and magnesium fluoride, as well as $MgF_2$–$AlF_3$ and $AlF_3$–LiF mixtures, in the neutron energy range between 0.6 meV and 1 keV. The neutron scattering properties have been investigated as a function of temperature, between 10 and 370 K, and sample microscopic structure, focusing in particular on differences between powder and sintered samples. Concurrent measurements of neutron transmission, neutron diffraction, neutron resonance capture analysis, and neutron Compton scattering provide a comprehensive picture of scattering and transport properties of these materials. We provide crystallographic information at the atomic scale, the effect of sintering on the grain size at the nanometer scale, the related occurrence of small angle scattering, and the impact of fluorine zero-point nuclear energy at different temperatures, requiring the use of an effective temperature to model its scattering within the impulse approximation. Finally, combining this self-consistent experimental information, we discuss the application of the uncertainty principle to the fluorine single-particle potential.



## I. INTRODUCTION

Boron Neutron Capture Therapy (BNCT) is a non-invasive form of binary radiotherapy that combines low-energy neutron irradiation with a boron-enriched drug, which preferentially accumulates in cancer cells.[1] The rationale of the treatment lies in the high cross section of thermal neutron capture in $^{10}B$, which releases two high-LET (Linear Energy Transfer), low-range charged particles. These particles cause lethal damage to the cells where the reaction takes place. The overall effect of the irradiation is thus the selective inactivation of the tumor, while sparing the surrounding healthy tissues. A new BNCT facility is being built in Italy, based on a

5 MeV, 30 mA radio frequency quadrupole proton accelerator, in the framework of the PNC-PNRR-ANTHEM project.[2] The interaction of protons with a beryllium target produces a high flux of neutrons, which are then filtered, moderated, and collimated within the Beam Shaping Assembly (BSA) to ensure the desired clinical beam. A beam with the appropriate energy spectrum for the treatment of deep-seated tumors is obtained by means of a BSA, having solid lithium-containing aluminum fluoride as a main constituent. Since aluminum fluoride ($AlF_3$) exists only in powder form, a novel sintering process was developed to densify a mixture of $AlF_3$ and lithium fluoride (LiF).[3,4] Moreover, to improve the mechanical properties of sintered-containing $AlF_3$ mixtures, a combination with $MgF_2$ has been considered, which also provides additional options for the design of BSA in BNCT facilities. Indeed, the construction of the BSA cannot only rely on thermalization properties, but it must also consider mechanical constraints and the ability to obtain elements with high-density and stable properties.

The robust design and efficacy of the BSA rely on the purity of the materials used and their characterization to validate neutron transport modeling in simulation codes. The activation of trace elements in the materials used for the BSA, following high-fluence neutron irradiation in the BNCT facility, may constitute a problem concerning their activation and the associated radiation-protection procedures. The presence of impurities was investigated using Neutron Activation Analysis (NAA) in the research reactor Triga Mark II at L.E.N.A. (Laboratorio Energia Nucleare Applicata) of the University of Pavia, indicating the suitability of industrial-grade samples for the BNCT facility.[5–7] Moreover, the energy spectrum of the neutron beam depends on the epithermal and thermal scattering cross sections, which, in turn, depend on the presence of resonances (epithermal region) and on the atom structure and dynamics within the condensed phases of a given material. Therefore, the amount of LiF in the BSA required to absorb the unwanted thermal component of the neutron beam can be optimized through Monte Carlo simulations based on accurate thermal scattering cross section libraries, i.e., material-dependent models that benefit from experimental validations.

Here, we present a self-consistent experimental approach for the determination of the total scattering cross section of $AlF_3$-, $MgF_2$-, and LiF-based compounds, through neutron diffraction and spectroscopy investigation of powder and sintered samples, as a function of temperature. Combining structural and dynamical information, we also discuss the fluorine single-particle quantum motion and the application of the uncertainty principle in this system.

## II. MATERIALS AND METHODS

### A. Sample preparation

Samples were prepared using the TT_SINTER machine developed by the INFN Unit of Pavia in collaboration with the University of Pavia.[8] Each sample powder is weighed and then used to fill a graphite mold that is used to shape the sintered materials. The graphite mold is then inserted into the TT_SINTER machine, where a cycle of heat and pressure gradients is applied to densify the powders. The specifics of such a cycle are subject to a non-disclosure agreement and, therefore, will not be included in this work. Nonetheless, the maximum temperature and pressure applied by the machine to obtain the sintered samples of $AlF_3$, $MgF_2$, $MgF_2$–$AlF_3$, and $AlF_3$–LiF are presented in Table I.

**TABLE I.** Maximum temperature ($T_{max}$) and pressure ($P_{max}$) of the sintering process for each material.

| Sample | $T_{max}$ (K) | $P_{max}$ (MPa) |
|---|---|---|
| $MgF_2$ | 1058.15 | 30.6 |
| $MgF_2$ + $AlF_3$ | 1023.15 | 30.6 |
| $AlF_3$ | 1173.15 | 35.7 |
| $AlF_3$+LiF | 918.15 | 30.6 |

Experiments were performed on $AlF_3$ and $MgF_2$ samples, in both the sintered and powder forms. In addition, sintered samples of $MgF_2$–$AlF_3$ and $AlF_3$–LiF were investigated.

### B. Neutron experiments

Experimental measurements[9] were performed at the VESUVIO beamline at the ISIS Neutron and Muon Source (UK).[10,11] Experiments were performed concurrently combining neutron transmission, neutron diffraction, neutron resonance capture analysis (NRCA), and neutron Compton scattering (NCS) (also referred to as deep inelastic neutron scattering).[12] Experiments were performed within the VESUVIO closed-circuit refrigerator, in the temperature region between 10 and 370 K.

Neutron transmission measurements were performed under white beam conditions in time-of-flight (TOF) mode. The pulsed operation of the ISIS facility allows the collection of data on VESUVIO in two TOF windows,[11] between 0.5 $\mu$s and 20 ms, corresponding to the energy range between hundreds of keV and 2.7 meV and between 20 and 40 ms, corresponding to the energy range between 2.7 and 0.6 meV. The measurement in the latter interval is not optimized, and the neutron flux is much lower, resulting in worse statistics in the collected spectra.

Neutron powder diffraction patterns were collected on VESUVIO, and data were analyzed in the TOF domain. A silicon standard (SRM-640c from NIST[13]) was employed to refine the instrument parameters, including the profile function for TOF data.[14] Rietveld refinements were carried out using the GSAS-II suite v5.5.[15] We refined atomic positions and isotropic displacement parameters for the $MgF_2$ (s.g. $P4_2/mnm$) and $AlF_3$ (s.g. $R\bar{3}c$) phases,[16,17] as well as microstrain and grain size parameters. A suitable Chebyshev polynomial was used to fit the incoherent background.

Neutron Resonance Capture Analysis (NRCA) was performed in TOF using the yttrium aluminum perovskite detectors at the instrument, with a lower-level discrimination threshold at 600 keV to suppress the environmental background within the instrument blockhouse.[18]

Neutron Compton Scattering (NCS) measurements were performed both in forward and in backward scattering regimes, the former to detect the presence of hydrogen in the samples[19] and the latter to measure the momentum distribution of fluorine within the samples, obtaining the value of its nuclear kinetic energy.[20] Within the impulse approximation[21,22] at epithermal energies, the double

scattering cross section, in the solid angle $d\Omega$ and at the final energy $dE'$, can be related to the dynamic structure factor,

$$\frac{d^2\sigma}{d\Omega dE'} = \sqrt{\frac{E'}{E}} \sum_j N_j \frac{\sigma_j}{4\pi} S_{IA,j}(Q, \Delta E), \tag{1}$$

modeled as the sum of single-nucleus neutron Compton profiles (NCPs), $J(y)$,

$$S_{IA,j}(Q, \Delta E) = \frac{M_j}{\hbar Q} J(y_j), \tag{2}$$

where $E$ is the neutron initial energy, $Q$ and $\Delta E$ are the neutron wavenumber and energy transfers, respectively, $M_j$ is the mass of the isotope $j$, $N_j$ is the number of such isotopes per formula unit, $\sigma_j$ is their bound scattering cross section,

$$y_j = \frac{M_j}{\hbar^2 Q}(\Delta E - E_{r,j}) \tag{3}$$

is the West-scaling variable for each isotope $j$, and $E_{r,j} = \frac{\hbar^2 Q^2}{2M_j}$ is the nucleus recoil energy. The second moment of the NCP, which can be approximated at a first order as a Gaussian function, is related to the average nuclear mean kinetic energy through the following relation:

$$\langle E_k \rangle_j = \frac{3\hbar^2}{2M_j} \int_{-\infty}^{\infty} y_j^2 J(y_j) dy_j. \tag{4}$$

The values of the fluorine $\langle E_K \rangle$ were fitted from the NCS data from the backward-scattering VESUVIO detectors.

### C. Cross section modeling

Modeling of thermal neutron scattering was obtained within the NCrystal environment.[23] This library, with its associated tools, allows for the computation of thermal neutron cross sections using crystallographic data as an input. Here, Bragg edges were modeled using the CIF files obtained within the analysis of the concurrent diffraction measurements.

Small angle neutron scattering (SANS) was approximated by representing the crystals as homogeneous spheres of radius R and assuming the related scattering processes as both elastic and coherent. The differential scattering cross section can be generally written as[24]

$$\left(\frac{d\sigma}{d\Omega}\right)_{\text{coh}} = N\langle |A(Q)|^2 \rangle, \tag{5}$$

where $N$ is the number of grains in the sample and $A(Q)$ is the scattering form factor, defined as

$$A(\mathbf{Q}) = \sum_l \tilde{b}_l e^{i\vec{Q}\cdot\vec{R}_l} = \int_0^R n_b e^{i\mathbf{Q}\cdot\mathbf{r}} d\mathbf{r}, \tag{6}$$

where the latter equality holds for a homogeneous sphere of radius $R$. The scattering length density is defined as $n_b = \frac{\sum_l \tilde{b}_l}{v}$, where $v$ is the volume of the unit cell and $l$ runs over all the atoms that compose a unit cell.

The analytical integration over $\vec{r}$ and the scattering angle $\theta$ yields an overall SANS cross section, which can be written as

$$\sigma_{SANS} \approx \left(\frac{4}{3}\pi R^3 n_b\right)^2 \frac{9\pi N \hbar^2}{8 m_N E\, R^2}. \tag{7}$$

The contribution per unit cell can be obtained, for $N = 1$, by considering that the number of unit cells inside a grain is $n = \frac{4\pi R^3}{3v}$. One obtains the characteristic $1/E$ SANS scattering cross section,[25]

$$\sigma_{\text{u.c.}} = f_R \frac{3\pi^2 v\, n_b^2\, \hbar^2 R}{2 m_N E}. \tag{8}$$

As the real sample is expected to contain a distribution of grain sizes, the above-mentioned formula needs to be weighted by a factor $f_R$, representing the fraction of such spheres within the sample.

Finally, absorption cross sections, particularly important in the case of Li-containing compounds through the $^6$Li isotope, were included as

$$\sigma_{abs}(E) = \sigma_{abs}(E_0)\sqrt{\frac{E_0}{E}} \tag{9}$$

using the reference absorption values at $E_0 = 25.3$ meV from Ref. 26.

## III. RESULTS AND DISCUSSION

### A. Thermal cross section

Neutron powder diffraction refinement was performed on sintered and powder samples of $AlF_3$ and $MgF_2$. In general, diffraction data showed broader Bragg peaks for the powders and narrower ones for the sintered samples. Profile analysis provided an estimate of the average effective crystalline size of the $AlF_3$ powder of the order of 14 nm and of several micrometers for the sintered sample. A larger domain size in the sintered samples is expected, as in the sintering process, the powder is subject to high pressure and temperature, which facilitates the crystal growth process. The sintering process, however, did not show significant changes in the position of the Bragg peaks, suggesting that procedure-related stress/strain effects on the total cross section can be neglected. It is important to notice that nanometer-size crystals, in completely coherent scattering systems like these, are expected to result in a strong SANS component of the total neutron cross section, as discussed later.

Additional measurements were performed on the sintered $AlF_3$–$MgF_2$ physical mixtures as a function of temperature. The results of the *in situ* experiment are reported in Figs. 1 and 2. For both phases, the average domain size parameters converged to a high value and were then fixed to 10 $\mu$m. Uniaxial microstrain parameters $\left(\frac{\Delta d}{d}\right)_\perp$ and $\left(\frac{\Delta d}{d}\right)_\parallel$, on the other hand, showed some level of lattice disorder and were refined to $0.6(7)\cdot 10^{-3}$ and $1.8(1)\cdot 10^{-3}$ for $MgF_2$ and $6.6(3)\cdot 10^{-3}$ and $4.4(1)\cdot 10^{-3}$ for $AlF_3$. Overall, the diffraction results suggest that one can effectively treat the $MgF_2$–$AlF_3$ sintered composite as a simple sum of the two components, as no significant change in the positions of the Bragg peaks was observed. Lattice parameters from the neutron diffraction analysis are summarized in Table II, while Table III reports the fractional coordinates of all atoms within the unit cells of the sintered $AlF_3$ and $MgF_2$ compounds. These positions, in the case of $AlF_3$–$MgF_2$, change on the last significant digit.

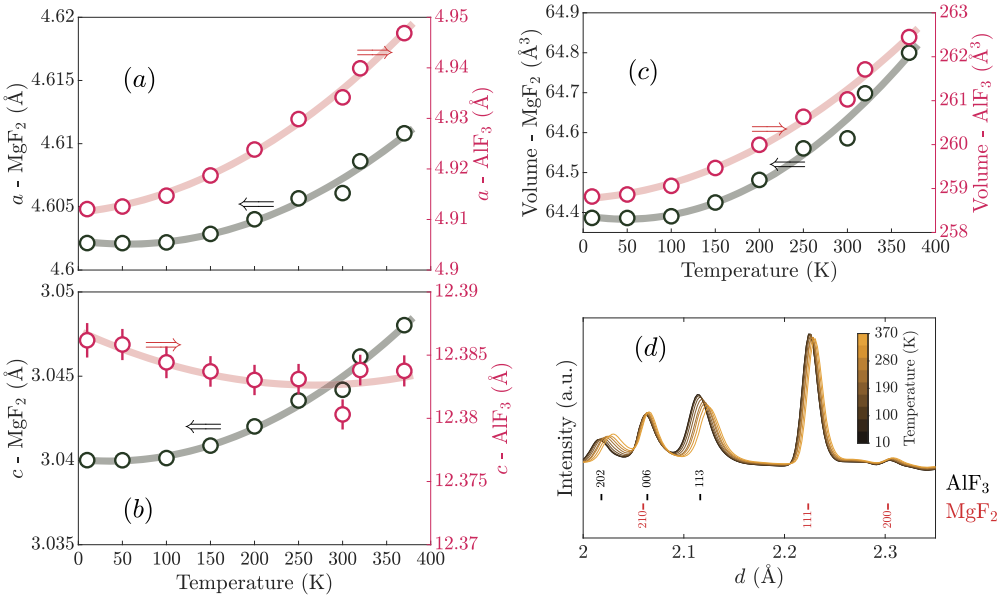


**FIG. 1.** *In situ* lattice expansion of the $MgF_2$–$AlF_3$ sintered sample. *a*-, *c*-lattice parameters and volume are reported (in red for $AlF_3$ and in black for $MgF_2$), respectively, in *a*, *b*, and *c*. Solid lines are fit to second-order polynomials. (d) Detail of the TOF pattern upon temperature evolution (indexed peaks for the two phases are highlighted by vertical tick marks and labeled).

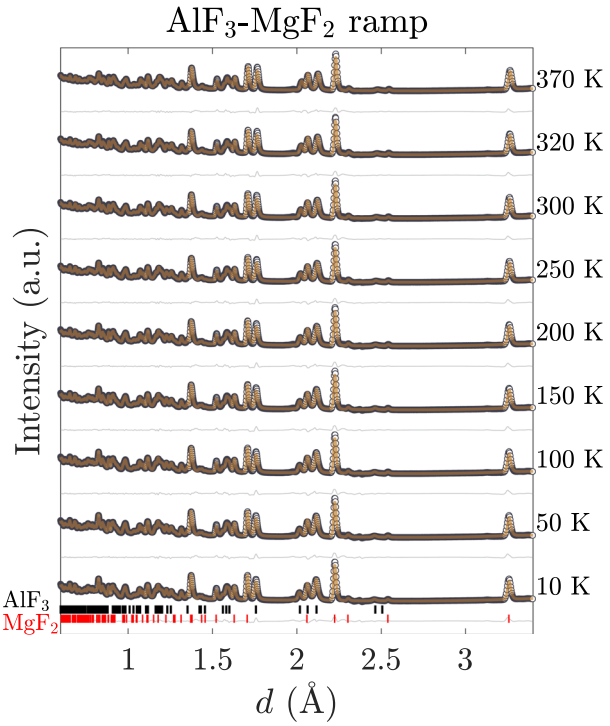


**FIG. 2.** *In situ* Rietveld refinement of the $AlF_3$–$MgF_2$ sintered sample. The data ($I_{obs}$), calculated pattern ($I_c$), and difference plot ($I_{obs}$–$I_c$) are reported, respectively, as black circles and orange and gray solid lines (average $R_{wp}$ = 2.74%, 56(3)-44.0(3) average wt. %).

**TABLE II.** Unit cell parameters ($a = b$ and $c$; $\alpha = \beta = 90°$ and $\gamma = 90°$ for tetragonal and 120° for rhombohedral), cell volume ($v$), and space group information from the analysis of neutron diffraction experiments on sintered samples at room temperature.

| Material | $a$ (Å) | $c$ (Å) | $v$ (Å$^3$) | Space group |
|---|---|---|---|---|
| $MgF_2$ | 4.6389(4) | 3.0420(4) | 65.463(8) | P $4_2$/m n m |
| $AlF_3$ | 4.9602(7) | 12.396(2) | 264.13(4) | R $\bar{3}$ c |
| $MgF_2$ in $MgF_2$–$AlF_3$ | 4.6061(2) | 3.0442(2) | 64.585(4) | P $4_2$/m n m |
| $AlF_3$ in $MgF_2$–$AlF_3$ | 4.9342(4) | 12.380(1) | 261.03(3) | R $\bar{3}$ c |

**TABLE III.** Fractional atomic coordinates of $AlF_3$ and $MgF_2$ as obtained from the crystallographic structures of the $MgF_2$ + $AlF_3$ compound at room temperature.

| $AlF_3$ | | | |
|---|---|---|---|
| Element | x/*a* | y/*b* | z/*c* |
| Al | 0 | 0 | 0 |
| F | 0.4252 | 0 | 1/4 |
| $MgF_2$ | | | |
| Element | x/*a* | y/*b* | z/*c* |
| Mg | 0 | 0 | 0 |
| F | 0.3024 | 0.3024 | 0 |

Transmission in the energy range between 0.6 meV and 1 keV for the sintered $MgF_2$–$AlF_3$ sample is reported in Fig. 3, as an example of the quality of the data collected. Transmissions for all samples considered showed a constant and featureless spectrum for

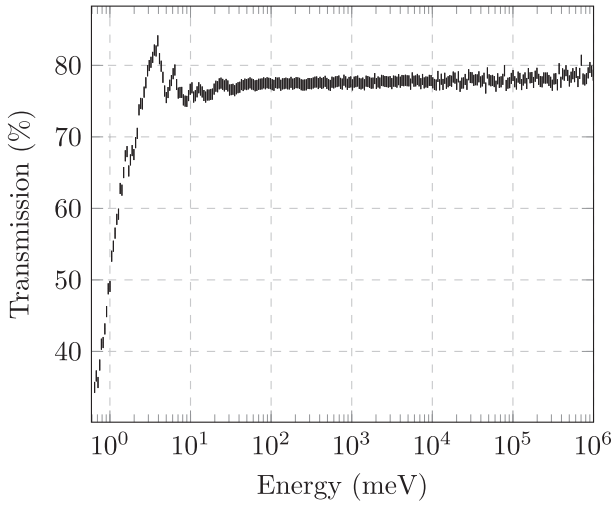


**FIG. 3.** Neutron transmission of the $AlF_3MgF_2$ sintered sample at 300 K.

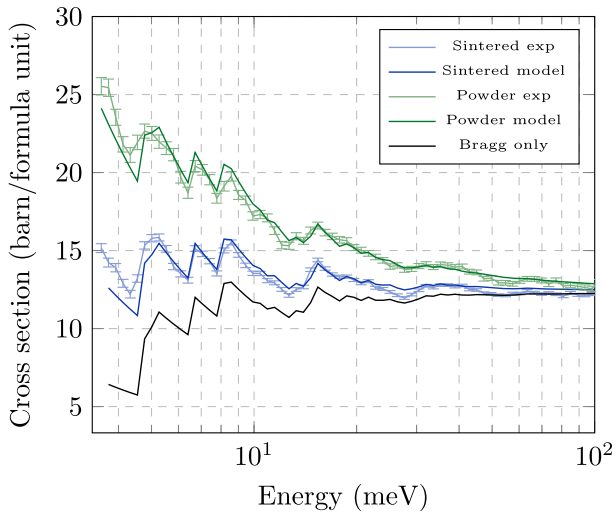


**FIG. 4.** Experimental total neutron cross section, per formula unit, of $AlF_3$ samples in the powder form (green error bars) and sintered disk (blue error bars). Models combining SANS and Bragg-edge scattering are reported as blue and green lines and are compared with the Bragg-edge scattering component, reported as a black solid line.

epithermal neutrons. In particular, no neutron resonances were found, both in neutron transmission and in NRCA measurements, over the explored epithermal energy range. This result shows that any impurities within the samples can be neglected in relation to the neutron transport properties.

Experimental neutron transmission spectra were converted into energy-dependent total cross section spectra, provided on an absolute scale as a barn/formula unit, based on the possibility to normalize the data in the sum of the free scattering cross sections in the epithermal region, as discussed in Ref. 27. The application of this procedure was based on the following two experimental conditions: (i) there are no nuclear resonances on a broad energy range (here we considered 10 eV–1 keV) and (ii) the stoichiometry of the sample is well known. The stoichiometry of the $MgF_2$–$AlF_3$ sample was tested against the results of the neutron diffraction refinements, which provided a stoichiometric ratio of Al:Mg = 0.939, in good agreement with the expected preparation ratio of 1. Moreover, the presence of water or other hydrogen-containing molecules in the samples, which would have an important effect on their neutron transport and moderation properties, was tested through NCS measurements, which showed no hydrogen signal within the limit of detection of the instrument[19] for all sintered samples and for the $AlF_3$ powder. Some hydrogen, likely from water, was observed in the $MgF_2$ powder, which was also observed as an incoherent background during the refinement of the neutron diffraction data.

Thermal neutron cross sections, presented below as a function of the incident neutron energy, include contributions from the crystal structure (evaluated in NCrystal), SANS [Eq. (8)], and neutron absorption [Eq. (9)]. Inelastic scattering contributions and temperature dependence are also included using NCrystal. It is useful to note that, with the exception of LiF–$AlF_3$, the samples have negligible contributions from neutron absorption, and the total cross sections are hence dominated by the scattering contributions.

Figure 4 shows the experimental total scattering cross section of $AlF_3$ powder and sintered samples, as green and blue error bars, respectively, focusing on the thermal energy region. The experimental spectra are modeled by combining a $1/E$ SANS component, fitted to the experimental data, with a sawtooth-like contribution due to coherent Bragg scattering, resulting in sharp Bragg edges. Based on the unit-cell parameters, the values of $n_b$ for $AlF_3$ and $MgF_2$ are $4.69 \times 10^{-6}$ Å$^{-2}$ and $1.55 \times 10^{-5}$ Å$^{-2}$, respectively. A comparison with a contribution from Bragg-scattering only is provided by the black solid line. As anticipated by the diffraction refinement, $AlF_3$ features a strong SANS contribution in the powder form, which is partially attenuated after the sintering procedure, although not at all negligible. The amount of SANS to be expected in these samples, however, is strongly dependent on the pristine powder used and on the sintering process, which can hardly be estimated without a direct neutron experiment. Moreover, from the transmission experimental data, one cannot directly access the grain radius, $R$, but rather the product $f_R R$ weighted by the fraction of R-sized grains within the samples, allowing only for a qualitative comparison with the diffraction results.

Figure 5 shows a comparison of the experimental total neutron scattering cross section of the sintered disks, specifically $AlF_3$ (blue error bars), $MgF_2$ (red error bars), and the mixture of the two. The SANS contribution was found to be higher in $AlF_3$ than in $MgF_2$, for both powder and sintered samples. In the case of the composite sample, the intensity of the SANS contribution is found to be larger than that of $MgF_2$ and smaller than that of $AlF_3$, as one could expect. It is interesting to notice that the trend in the SANS intensities of the three samples seems to correlate with the trend of their densities relative to the bulk materials, as reported in Table IV. In fact, in a sample with an important component of nanometer-sized spherical grains, the packing fraction would be significantly lower than one. As a qualitative comparison, the packing fraction for a system of spheres of constant dimensions is about 74%. Figure 5 also shows a

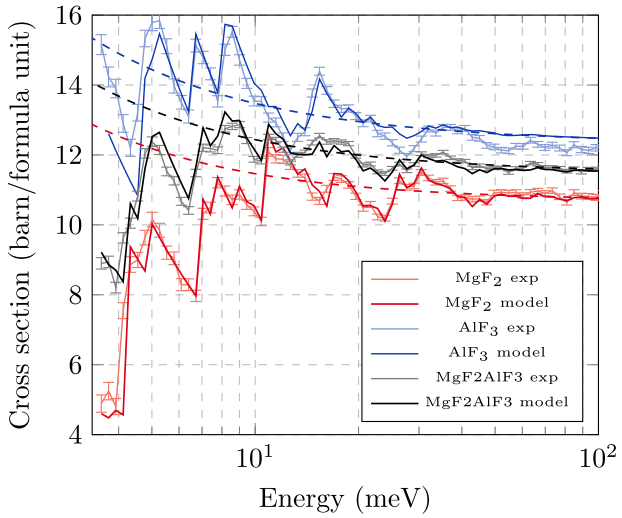


**FIG. 5.** Experimental total neutron cross section, per formula unit, for the sintered samples of $AlF_3$ (blue error bars), $MgF_2$ (red error bars), and $AlF_3MgF_2$ (black error bars), together with the corresponding modeling (solid lines) combining coherent SANS and Bragg-edge contributions. The dashed lines correspond to the evaluated total cross sections using nuclear libraries (ENDF.B/VIII[28]), not including structural or dynamical effects at the atomic scale.

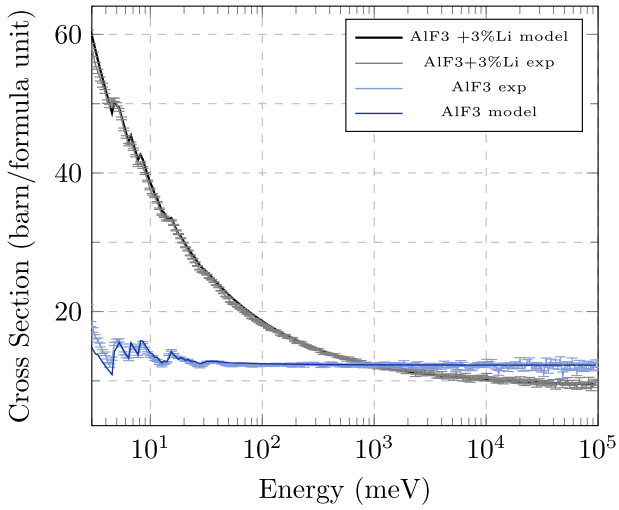


**FIG. 6.** Total cross section of the $AlF_3$ sintered samples, with (black error bars) and without (blue error bars) 3 wt. % of LiF.

comparison with typical nuclear cross sections not including structural and dynamical effects at the atomic scale. The reported evaluated cross sections are printed as dashed lines for $AlF_3$, $MgF_2$, and the mixture of the two. They are taken from ENDF.B/VIII,[28] combining the nuclear cross section for each isotope in the compounds, and have the typical behavior of a gas of non-interacting nuclei at a given temperature, used in any Monte Carlo code not using material-specific thermal neutron cross sections. For the materials investigated here, whose scattering properties are dominated by coherent and elastic neutron scattering, the most evident difference is the absence of the Bragg-related interference effects, which require interaction on the atomic scale to hold atoms at their average crystal positions.

Finally, Fig. 6 shows the comparison of the total cross section of the $AlF_3$ samples, with and without the addition of LiF. The lithium-containing sample is well reproduced by a model including the thermal Bragg scattering and the dominant contribution from the $^6$Li absorption cross section, which has a characteristic dependence on $1/\sqrt{E}$. The marked SANS contribution from $AlF_3$, clearly visible in the sintered disk without lithium, does not seem to be present in the cross section of the lithium-containing sample. One should note that the two contributions have different neutron-energy dependencies, with the SANS cross section, dependent on $1/E$, increasing more rapidly as the neutron energy decreases.

## B. Epithermal cross section

At epithermal energies, the neutron scattering is dominated by incoherent and inelastic processes, and the double-differential cross section can be expressed as in Eq. (2). However, the shape of the NCP still depends upon the interatomic interactions of the system. The main effect is that the nuclear kinetic energy of each atom increased with respect to the Maxwell–Boltzmann (M.B.) prediction within a perfect-gas framework, namely $3/2k_BT$. The main reason for an increased value of $\langle E_K \rangle$ is the existence of zero-point vibrational energies, which are often neglected in computer simulations for isotopes heavier than protium.

Figure 7 (top) shows the raw experimental NCS data within the fluorine $y_F$ scaling variable. The NCP has the physical interpretation of the distribution of the nuclear momenta $\vec{p}$ probed along the scattering wave vector transfer, $y_F = \vec{p} \cdot \hat{Q}$. We note that, in the current notation, nuclear momenta are expressed in terms of wave vectors

**TABLE IV.** Physical properties of different samples.

| Sample | Mass (g) | Thickness (mm) | Meas. density (g/cm$^3$) | Rietveld density (g/cm$^3$) | Rel. density (%) |
|---|---|---|---|---|---|
| $MgF_2$ | 37.992 | 6.35 | 3.05 | 3.17 | 96 |
| $MgF_2$ + $AlF_3$ | 54.857 | 9.85 | 2.86 | 3.20 | 84 |
| $AlF_3$ | 49.488 | 11.25 | 2.42 | 3.19 | 76 |

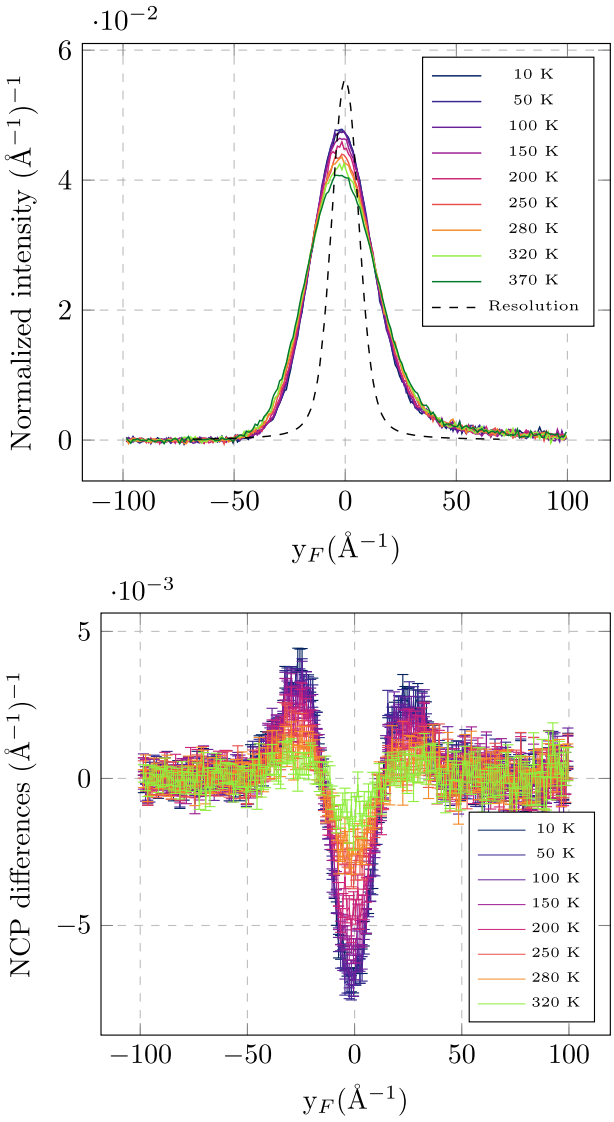


**FIG. 7.** Top: Raw NCS data from the $MgF_2$–$AlF_3$ composite in the fluorine y-space domain, at several experimental temperatures, together with the NCS resolution function (black dashed line). Bottom: Differences of NCS spectra at different temperatures with respect to the 370 K spectrum.

with units of $Å^{-1}$. Therefore, the profile needs to be a symmetric function of $y_F$, dynamically centered along the recoil line $\Delta E = E_r$. As the scattering of epithermal neutrons is dominated by fluorine, the raw data provide a peak profile well centered around $y_F = 0$. However, additional scattering contributions, such as multiple scattering, scattering from Mg, and scattering from Al, in order of magnitude, amount to about 43% of the overall intensity. The spectral changes observed in Fig. 7 are expected to be solely related to the change in the fluorine NCP, while the other contributions provide (in the $y_F$ domain) a temperature-independent background. This is because only the single-scattering from fluorine, i.e., *the fluorine NCP*, scales according to the $y_F$ variable, preserving the temperature dependence of the momentum distribution when the spectra from all the detectors are summed together. Meanwhile, multiple scattering and single scattering from other masses do not scale according to $y_F$, and any temperature-induced change in their contribution becomes negligible when spectra from different detectors are summed together. This behavior, originally discussed in Ref. 29, was also checked against Monte Carlo simulations during data analysis. For this reason, and following the discussion in Ref. 29, one can extract the mean kinetic energy directly from the difference spectra, featuring characteristic oscillations that can be appreciated in Fig. 7 (bottom).

The experimental values of the fluorine $\langle E_K \rangle$ in the $MgF_2$–$AlF_3$ mixture are reported in Fig. 8 and Table V. Any comparison with the classical M.B. prediction is due to fail, as the fluorine $\langle E_K \rangle$ is about 20% higher than the classical value still at 370 K, and the difference clearly increases as one goes to lower temperatures, where quantum zero-point vibrational energies dominate. To obtain more suitable comparisons,[21] one can use the virial theorem and the knowledge of a Vibrational Density of States (VDOS), $g(\omega)$. In particular, one has

$$\langle E_K \rangle = \frac{3\hbar}{4} \int_0^\infty \omega g(\omega) \coth\left(\frac{\hbar\omega}{2k_B T}\right) d\omega. \tag{10}$$

A VDOS for $MgF_2$ was provided within the NCrystal data library,[23] which contains data reported in Refs. 16 and 30, and the result of numerical integrations of Eq. (10) provides the results (labeled as VDOS) in Fig. 8 and Table V. In addition, we provide a prediction from a simplified Debye-like VDOS of the following form:

$$g_D(\omega) = \frac{3\hbar^2\omega^2}{(k_B T_D)^3} \tag{11}$$

with an *ad hoc* Debye temperature of $T_D = 590$ K. A similar approach was presented, for example, in Ref. 31, where a Debye

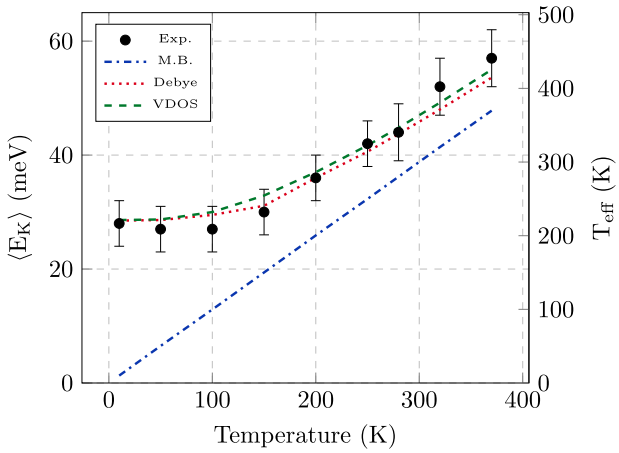


**FIG. 8.** Experimental (black error bars) nuclear mean kinetic energy of fluorine in the $MgF_2$–$AlF_3$ composite, together with the Maxwell–Boltzmann free-gas prediction (blue dotted-dashed line), a Debye model with a characteristic temperature of 590 K, and calculated from the vibrational density of states provided in Refs. 16 and 30.

**TABLE V.** Fluorine nuclear mean kinetic energy, $\langle E_K \rangle$, in meV, from the NCS measurements (Expt.) on the $MgF_2$–$AlF_3$ mixture, within a classical Maxwell–Boltzmann (M.B.) framework, for a Debye solid with a characteristic temperature of 590 K (Debye), and from the vibrational density of states calculated in Refs. 16 and 30 (VDOS).

| T (K) | Expt. | M.B. | Debye | VDOS |
|---|---|---|---|---|
| 10 | 28 ± 4 | 1.3 | 28.5 | 28.6 |
| 50 | 27 ± 4 | 6.5 | 28.6 | 28.7 |
| 100 | 27 ± 4 | 12.9 | 29.5 | 30 |
| 150 | 30 ± 4 | 19.4 | 31.1 | 32.9 |
| 200 | 36 ± 4 | 25.9 | 36.0 | 37.0 |
| 250 | 42 ± 4 | 32.3 | 40.6 | 41.7 |
| 280 | 44 ± 5 | 36.2 | 43.7 | 44.8 |
| 320 | 52 ± 5 | 41.4 | 48.0 | 49.2 |
| 370 | 57 ± 5 | 47.8 | 53.6 | 55.0 |

model was favorably compared to path-integral molecular dynamics simulations in the case of Li dynamics. One can notice how both predictions, corresponding to different levels of theory, provide consistent results with the experimental values, as well as a much more suitable description than the classical one. It is useful to note that the experimental mean kinetic energy can be converted into an effective temperature of the following form:

$$T_{eff} = \frac{2\langle E_K \rangle}{3k_B} > T, \tag{12}$$

always larger than the thermodynamic temperature of the system, $T$. Therefore, when modeling the neutron scattering at epithermal energies, one can obtain more accurate results by imposing $T_{eff}$ as the system temperature, which has the effect of broadening the scattering kernel response function,

$$\frac{d^2\sigma}{d\Omega dE'} = \sqrt{\frac{E'}{E}}\frac{\sigma_F}{4\pi}\frac{\exp\left(-\frac{(\Delta E - E_r)^2}{4E_r k_B T_{eff}}\right)}{\sqrt{4\pi E_r k_B T_{eff}}}. \tag{13}$$

In recent years, several NCS investigations have provided experimental evidence of the quantum motion of nuclei heavier than hydrogen, e.g., oxygen in water and $BaZrO_3$, as presented in Refs. 32–34. More specifically, experimental and theoretical values for the fluorine nuclear mean kinetic energy were provided in Ref. 35, which are qualitatively similar and have the same temperature behavior as those reported here.

### C. The uncertainty principle on fluorine dynamics

A final remark should be spent on the application of the uncertainty principle on the single-particle dynamics of fluorine,

$$u^2 p^2 \geq \frac{1}{4}, \tag{14}$$

with $u^2$ being the mean square displacement and $p^2$ being the mean square momentum, representing the spatial and momentum uncertainties on the nuclear dynamics in a solid. As the uncertainty principle should be minimized for a harmonic potential, any deviation from such a picture can be related to deviations from such an assumption. Interestingly, the experimental results presented provide experimental values for both observables. A determination of the isotropic mean square displacement is obtained by the Rietveld refinement of the diffraction data. At the same time, a determination of the isotropic mean square momentum is obtained from NCS, as $p^2 = \langle y_F^2 \rangle$. The experimental values for both observables, as a function of temperature, are provided in Table VI. For an ideal Einstein solid of characteristic energy $\hbar\omega_E$, corresponding to an isotropic and a harmonic potential, the uncertainty principle could be rewritten, as a function of temperature, as

**TABLE VI.** Experimental values for the isotropic mean square displacement ($u^2$, from the Rietveld refinement) and mean square momentum $p^2 = \langle y_F^2 \rangle$, together with the predictions from the Debye model with a characteristic temperature of 590 K and from the VDOS of bulk $MgF_2$.

| T (K) | $u^2_{exp}$ ($10^{-4}$ Å$^2$) | $p^2_{exp}$ (Å$^{-2}$) | $4(u^2p^2)_{exp}$ | $4(u^2p^2)_D$ | $4(u^2p^2)_{VODS}$ |
|---|---|---|---|---|---|
| 10 | 56 ± 2 | 70 ± 3 | 1.6 ± 0.1 | 1.1 | 1.2 |
| 50 | 52 ± 2 | 70 ± 3 | 1.5 ± 0.1 | 1.2 | 1.2 |
| 100 | 56 ± 2 | 73 ± 3 | 1.6 ± 0.1 | 1.4 | 1.5 |
| 150 | 64 ± 2 | 79 ± 4 | 2.0 ± 0.2 | 1.8 | 1.9 |
| 200 | 72 ± 2 | 86 ± 4 | 2.5 ± 0.2 | 2.3 | 2.6 |
| 250 | 81 ± 2 | 102 ± 4 | 3.3 ± 0.2 | 3.1 | 3.4 |
| 280 | 89 ± 2 | 109 ± 4 | 3.9 ± 0.2 | 3.6 | 4.0 |
| 320 | 96 ± 2 | 123 ± 4 | 4.8 ± 0.3 | 4.5 | 4.9 |
| 370 | 108 ± 2 | 142 ± 5 | 6.1 ± 0.3 | 5.6 | 6.2 |

$$(u^2p^2)_E = \frac{1}{4}\left(\coth\left(\frac{\hbar\omega_E}{2k_BT}\right)\right)^2, \tag{15}$$

which provides the familiar result of 1/4 at low temperatures, when the system is found in its fundamental state. Any other potential is bound to provide higher values, as one can appreciate from the Debye predictions, for a characteristic temperature of $T_D$ = 590 K, and based on the VDOS of $MgF_2$, provided in the same table. All models and experiments provide the same behavior of $4u^2p^2$ as a function of temperature. While both the Debye and VDOS models feature a low-temperature limit (1.1 and 1.2, respectively), higher than an Einstein model, the experimental result is significantly higher (1.6 ± 0.1). One should note that a very similar value (1.5) could be obtained in the case of oxygen in $BaZrO_3$ at low temperatures based on the results in Ref. 33. There, it was commented that, especially at low temperatures, the value of $u^2$ is likely to be overestimated because of other contributions to the Bragg-peak broadening due to disorder. However, as temperature increases and the real mean-square displacement contribution dominates any other contribution, the experimental value of $4u^2p^2$ and the predictions from the two models are in quantitative agreement.

## IV. CONCLUSIONS

We have provided an experimental validation of the scattering properties of $MgF_2$ and $AlF_3$ compounds for thermal and epithermal neutrons up to 1 keV. In particular, we have shown that $MgF_2$–$AlF_3$ mixtures retain similar structures as the composing crystal, which simplifies the modeling of coherent Bragg scattering. Moreover, we have found that the sintering process, which does

not show significant changes in the Bragg peak positions, has the effect of increasing the average crystal sizes with respect to those in the powder ingredients, thus decreasing small-angle scattering contributions, particularly relevant for $AlF_3$. We have confirmed that any impurities in the samples are in negligible amounts, specifically in relation to the presence of epithermal neutron resonances, and we have found that any hydrogen content is below the experimental limits of detection. Finally, we have measured the fluorine nuclear mean kinetic energy, showing that still at 370 K, its value is about 20% higher than the classical Maxwell–Boltzmann prediction. Kinetic energy values at different temperatures, between 10 and 370 K, were modeled from vibrational densities of states, showing that a simplified Debye model with a characteristic temperature of 590 K is suitable, at least compared with the present error bars.

In conclusion, we have shown that material-specific and preparation-specific measurements of thermal neutron cross sections are a crucial step for the benchmarking of computer simulations and that experiments at the VESUVIO spectrometer can provide a self-consistent picture of the structural and dynamical properties of the samples that characterize thermal scattering kernels.

## ACKNOWLEDGMENTS

The authors acknowledge the financial support from the Consiglio Nazionale delle Ricerche under the CNR-STFC Grant Agreement No. 2021–2027 concerning collaboration in scientific research at the ISIS (UK) of STFC. The STFC Rutherford Appleton Laboratory is acknowledged for access to neutron beam facilities. This work was also supported by the National Plan for NRRP Complementary Investments (PNC, established with the decree-law 6 May 2021, No. 59, converted by Law No. 101 of 2021) in the call for the funding of research initiatives for technologies and innovative trajectories in the health and care sectors (Directorial Decree No. 931 of 06 June 2022)—Project No. PNC0000003—AdvaNced Technologies for Human-centrEd Medicine (project acronym: ANTHEM). Partial support from the Spanish Institute of Health Carlos III under Project No. DTS22-00147 is also acknowledged. This work reflects only the authors' views and opinions; neither the Ministry for University and Research nor the European Commission can be considered responsible for them.

## AUTHOR DECLARATIONS

### Conflict of Interest

The authors have no conflicts to disclose.

### Author Contributions

**Margherita Simoni**: Data curation (equal); Formal analysis (equal); Investigation (equal); Methodology (equal); Validation (equal); Visualization (equal); Writing – original draft (equal); Writing – review & editing (equal). **Setareh Fatemi**: Conceptualization (equal); Investigation (equal); Methodology (equal); Validation (equal); Visualization (equal); Writing – original draft (equal); Writing – review & editing (equal). **Lorenzo Airoldi**: Investigation (equal); Methodology (equal); Writing – review & editing (equal). **Silva Bortolussi**: Conceptualization (equal); Funding acquisition (equal); Investigation (equal); Methodology (equal); Supervision (equal); Validation (equal); Visualization (equal); Writing – review & editing (equal). **Mattia Gaboardi**: Data curation (equal); Formal analysis (equal); Investigation (equal); Methodology (equal); Validation (equal); Visualization (equal); Writing – original draft (equal); Writing – review & editing (equal). **Matthew Krzystyniak**: Investigation (equal); Methodology (equal); Writing – review & editing (equal). **Anna Marsicano**: Investigation (equal); Methodology (equal); Writing – review & editing (equal). **Triestino Minniti**: Formal analysis (equal); Investigation (equal); Methodology (equal); Validation (equal); Writing – review & editing (equal). **Ignacio Porras**: Investigation (equal); Methodology (equal); Writing – review & editing (equal). **Ian Postuma**: Investigation (equal); Methodology (equal); Writing – review & editing (equal). **Ricardo Ramos**: Investigation (equal); Methodology (equal); Writing – review & editing (equal). **Roberto Senesi**: Conceptualization (equal); Investigation (equal); Methodology (equal); Supervision (equal); Validation (equal); Visualization (equal); Writing – review & editing (equal). **Umberto Anselmi Tamburini**: Investigation (equal); Methodology (equal); Writing – review & editing (equal). **Valerio Vercesi**: Funding acquisition (equal); Investigation (equal); Methodology (equal); Supervision (equal); Writing – review & editing (equal). **Giovanni Romanelli**: Conceptualization (equal); Data curation (equal); Funding acquisition (equal); Investigation (equal); Methodology (equal); Supervision (equal); Validation (equal); Visualization (equal); Writing – original draft (equal); Writing – review & editing (equal).

## DATA AVAILABILITY

The data that support the findings of this study are available from the corresponding author upon reasonable request.

## REFERENCES

[1] J. A. Coderre and G. M. Morris, "The radiation biology of boron neutron capture therapy," Radiat. Res. **151**, 1–18 (1999).

[2] A. Pisent *et al.*, "Anthem project, construction of a RFQ driven BNCT neutron source," in *Proceedings of the LINAC2024, International Linear Accelerator Conference No. 32*, Geneva, Switzerland, 2024, http://www.jacow.org, pp. 291–294.

[3] S. Bortolussi, "Boron Neutron Capture Therapy: a technological journey to bring neutrons in hospital," Il Nuovo Saggiatore, Vol. 39, anno 2023, no. 3-4. https://www.ilnuovosaggiatore.sif.it/article/348

[4] I. Postuma, S. González, M. S. Herrera, L. Provenzano, M. Ferrarini, C. Magni, N. Protti, S. Fatemi, V. Vercesi, G. Battistoni *et al.*, "A novel approach to design and evaluate BNCT neutron beams combining physical, radiobiological, and dosimetric figures of merit," Biology **10**, 174 (2021).

[5] R. R. Greenberg, P. Bode, and E. A. De Nadai Fernandes, "Neutron activation analysis: A primary method of measurement," Spectrochim. Acta, Part B **66**, 193–241 (2011).

[6] D. Alloni, A. Borio di Tigliole, A. Cammi, D. Chiesa, M. Clemenza, G. Magrotti, L. Pattavina, S. Pozzi, M. Prata, E. Previtali, A. Salvini, A. Sartori, and M. Sisti, "Final characterization of the first critical configuration for the TRIGA Mark II reactor of the University of Pavia using the Monte Carlo code MCNP," Prog. Nucl. Energy **74**, 129–135 (2014).

[7] C. Magni, M. Ferrarini, I. Postuma, N. Protti, S. Fatemi, C. Gong, U. Anselmi-Tamburini, V. Vercesi, G. Battistoni, S. Bortolussi *et al.*, "Neutron activation

and dosimetry studies for a clinical facility of boron neutron capture therapy," Il Nuovo Cimento **44C**, 135 (2021).
[8]INFN-PNC-PNRR-ANTHEM, "Tt_Sinter project description," https://web.infn.it/BNCT/tt_sinter/.
[9]G. Romanelli, T. Minniti, M. Simoni, R. L. Ramos, R. Senesi, I. Postuma, S. Bortolussi, and S. Fatemi, "Experimental validation of the neutron transport within a $AlF_3$ and $MgF_2$ neutron moderators for medical applications," ISIS Experiment No. RB2420139 (2025).
[10]J. Mayers and G. Reiter, "The VESUVIO electron volt neutron spectrometer," Meas. Sci. Technol. **23**, 045902 (2012).
[11]G. Romanelli, M. Krzystyniak, R. Senesi, D. Raspino, J. Boxall, D. Pooley, S. Moorby, E. Schooneveld, N. J. Rhodes, C. Andreani, and F. Fernandez-Alonso, "Characterisation of the incident beam and current diffraction capabilities on the VESUVIO spectrometer," Meas. Sci. Technol. **28**, 095501 (2017).
[12]G. Romanelli, M. Krzystyniak, G. Festa, C. Andreani, F. Fernandez-Alonso, and R. Senesi, "The road to a station for epithermal and thermal neutron analysis," J. Phys.: Conf. Ser. **1055**, 012017 (2018).
[13]R. J. Lewis, "National Institute of Standards and Technology," in *Hawley's Condensed Chemical Dictionary, September* (John Wiley and Sons, Inc., Hoboken, NJ, 2007), pp. 4–7.
[14]R. B. Von Dreele, J. D. Jorgensen, and C. G. Windsor, "Rietveld refinement with spallation neutron powder diffraction data," J. Appl. Crystallogr. **15**, 581–589 (1982).
[15]B. H. Toby and R. B. Von Dreele, "GSAS-II: The genesis of a modern open-source all purpose crystallography software package," J. Appl. Crystallogr. **46**, 544–549 (2013).
[16]W. H. Baur and A. A. Khan, "Rutile-type compounds. IV. $SiO_2$, $GeO_2$ and a comparison with other rutile-type structures," Acta Crystallogr., Sect. B **27**, 2133–2139 (1971).
[17]P. Daniel, A. Bulou, M. Rousseau, J. Nouet, J. L. Fourquet, M. Leblanc, and R. Burriel, "A study of the structural phase transitions in $AlF_3$: X-ray powder diffraction, differential scanning calorimetry (DSC) and Raman scattering investigations of the lattice dynamics and phonon spectrum," J. Phys.: Condens. Matter **2**, 5663–5677 (1990).
[18]D. Onorati, G. Romanelli, P. Ulpiani, C. Cazzaniga, E. Preziosi, L. Arcidiacono, G. Festa, C. Andreani, R. Senesi, and M. C. Morone, "FLUKA simulations and benchmark measurements of the YAP(Ce) scintillators installed on the VESUVIO spectrometer," Nucl. Instrum. Methods Phys. Res., Sect. A **969**, 164012 (2020).
[19]M. Krzystyniak, G. Romanelli, and F. Fernandez-Alonso, "Non-destructive quantitation of hydrogen via mass-resolved neutron spectroscopy," Analyst **144**, 3936–3941 (2019).
[20]C. Andreani, M. Krzystyniak, G. Romanelli, R. Senesi, and F. Fernandez-Alonso, "Electron-volt neutron spectroscopy: Beyond fundamental systems," Adv. Phys. **66**, 1–73 (2017).
[21]C. Andreani, R. Senesi, M. Krzystyniak, G. Romanelli, and F. Fernandez-Alonso, "Atomic quantum dynamics in materials research," in *Neutron Scattering – Applications in Biology, Chemistry, and Materials Science, Experimental Methods in the Physical Sciences Vol. 49*, edited by F. Fernandez-Alonso and D. L. Price (Academic Press, 2017), Chap. 7, pp. 403–457.
[22]V. F. Sears, "Scaling and final-state interactions in deep-inelastic neutron scattering," Phys. Rev. B **30**, 44–51 (1984).
[23]X.-X. Cai and T. Kittelmann, "NCrystal: A library for thermal neutron transport," Comput. Phys. Commun. **246**, 106851 (2020).
[24]F. Fernandez-Alonso and D. L. Price, *Neutron Scattering – Fundamentals* (Academic Press, New York, 2013).
[25]J. R. Granada, J. I. Márquez Damián, J. Dawidowski, J. I. Robledo, C. Helman, G. Romanelli, and G. Škoro, "Development of neutron scattering kernels for cold neutron reflector materials," J. Neutron Scattering **23**, 167 (2021).
[26]V. F. Sears, "Neutron scattering lengths and cross sections," Neutron News **3**, 26–37 (1992).
[27]J. I. Robledo, J. Dawidowski, J. I. Márquez Damián, G. Škoro, C. Bovo, and G. Romanelli, "Measurement of neutron total cross sections at the VESUVIO spectrometer," Nucl. Instrum. Methods Phys. Res., Sect. A **971**, 164096 (2020).
[28]D. A. Brown, M. B. Chadwick, R. Capote, A. C. Kahler, A. Trkov, M. W. Herman, A. A. Sonzogni, Y. Danon, A. D. Carlson, M. Dunn *et al.*, "ENDF/B-VIII.0: The 8th major release of the Nuclear Reaction Data Library with CIELO-project cross sections, new standards and thermal scattering data," Nuclear Data Sheets **148**, 1–142 (2018), part of Special Issue: Special Issue on Nuclear Reaction Data.
[29]G. Romanelli and M. Krzystyniak, "On the line-shape analysis of Compton profiles and its application to neutron scattering," Nucl. Instrum. Methods Phys. Res., Sect. A **819**, 84–88 (2016).
[30]Kyoto University, "Kyoto university database of phonon calculations," https://mdr.nims.go.jp/datasets/1c3552f6-be5d-42a4-a73d-ee485ca5ddc5.
[31]C. Filippi and D. M. Ceperley, "Path-integral Monte Carlo calculation of the kinetic energy of condensed lithium," Phys. Rev. B **57**, 252–257 (1998).
[32]G. Romanelli, M. Ceriotti, D. E. Manolopoulos, C. Pantalei, R. Senesi, and C. Andreani, "Direct measurement of competing quantum effects on the kinetic energy of heavy water upon melting," J. Phys. Chem. Lett. **4**, 3251–3256 (2013).
[33]A. Perrichon, E. Jedvik Granhed, G. Romanelli, A. Piovano, A. Lindman, P. Hyldgaard, G. Wahnström, and M. Karlsson, "Unraveling the ground-state structure of $BaZrO_3$ by neutron scattering experiments and first-principles calculations," Chem. Mater. **32**, 2824–2835 (2020).
[34]G. Romanelli, C. Andreani, A. Bocedi, and R. Senesi, "Quantum motion of oxygen and hydrogen in water: Atomic and total kinetic energy across melting from neutron scattering measurements," J. Chem. Phys. **160**, 234503 (2024).
[35]A. G. Seel, M. Ceriotti, P. P. Edwards, and J. Mayers, "Simultaneous measurement of lithium and fluorine momentum in $^7$LiF," J. Phys.: Condensed Matter **24**, 365401 (2012).